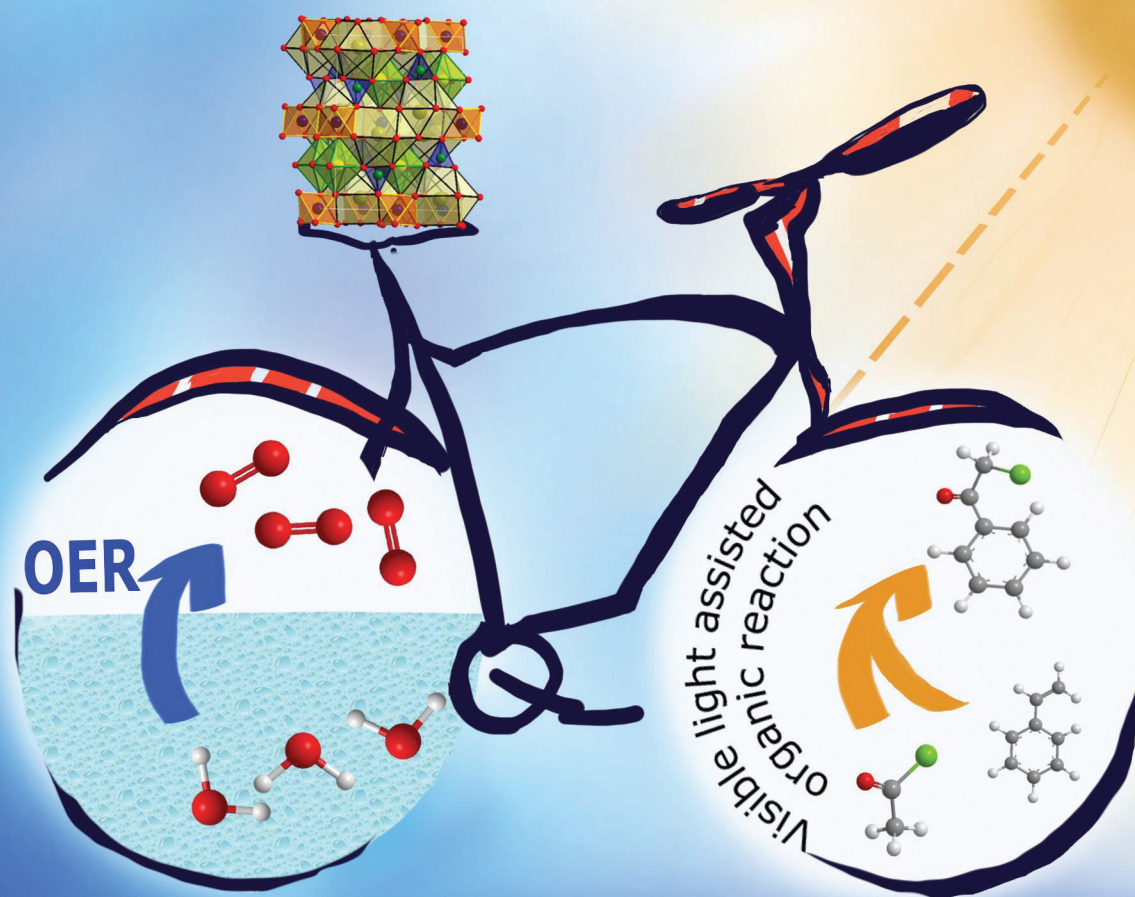


Dalton Transactions

An international journal of inorganic chemistry

rsc.li/dalton



ISSN 1477-9226

PAPER

Srinivasan Natarajan *et al.*
Synthesis, structure, oxygen evolution reaction (OER)
and visible-light assisted organic reaction studies on
 $A_2M_2TeB_2O_{10}$ (A = Ba and Pb; M = Mg, Zn, Co, Ni, Cu, and Fe)

Cite this: *Dalton Trans.*, 2025, **54**, 2753

Synthesis, structure, oxygen evolution reaction (OER) and visible-light assisted organic reaction studies on $A_2M_2TeB_2O_{10}$ (A = Ba and Pb; M = Mg, Zn, Co, Ni, Cu, and Fe)[†]

Indrani G. Shanmugapriya,[‡] Shreenibasa Sa[‡] and Srinivasan Natarajan *

Compounds with the general formula $A_2M_2TeB_2O_{10}$ (A = Ba and Pb; M = Mg, Zn, Co, Ni, Cu, and Fe) have been synthesised via solid-state techniques and characterised. The structure exhibits $M_2B_2O_{10}$ layers connected by TeO_6 octahedra giving rise to a three-dimensional structure with voids, where Ba^{2+} ions reside. Substitution of Mg by transition elements (M = Co, Ni, and Cu) in $Ba_2Mg_2TeB_2O_{10}$ and $(Ba_{0.5}Pb_{1.5})Mg_2TeB_2O_{10}$ gives rise to interesting colored compounds. NIR reflectivity studies indicated that white-colored compounds exhibited good NIR reflectivity, which was comparable to that of TiO_2 . Dielectric studies indicated reasonable values with low dielectric loss at low frequencies. The cobalt-substituted compounds $Ba_2(MgCo)TeB_2O_{10}$ and $(Ba_{0.5}Pb_{1.5})(MgCo)TeB_2O_{10}$ were explored towards the oxygen evolution reaction (OER) in an alkaline medium. The compound $(Ba_{0.5}Pb_{1.5})(MgCo)TeB_2O_{10}$ was found to be a good electrocatalyst for the OER with a faradaic efficiency of ~96%. The Cu-substituted compound $Ba_2(Mg_{1.5}Cu_{0.5})TeB_2O_{10}$ was found to be a good photocatalyst for the formation of α -chloroketones under visible light in the presence of molecular oxygen.

Received 24th September 2024,
Accepted 2nd December 2024

DOI: 10.1039/d4dt02706j

rsc.li/dalton

Introduction

Compounds based on borates have been explored over the years for their many properties in glasses, catalysis, non-linear optical materials and as a host for luminescence.¹ The oxyanions of boron have become one of the important constituents of solid-state chemistry.² Studies carried out on borate-containing compounds illustrate the rich diversity in their structural arrangement and properties.^{3,4} It is becoming clear that borate compounds with their unique structures, some of which are related to minerals,^{5,6} could be harnessed towards new advanced functional materials. The growth of borate-based compounds is so rapid that it is important to understand their structure–property–function relationships to provide guidance for future research. In order to conduct such a study, we considered a recently reported borate compound, $A_2Mg_2TeB_2O_{10}$ (A = Ba and Pb).⁷

Water splitting employing electrocatalysis has received much attention in recent years with many reviews summarizing its various aspects and highlighting its importance.^{8–10} Among the reactions, hydrogen evolution reactions (HERs) and oxygen evolution reactions (OERs) are the two most important reactions that are being actively pursued. Among the HER and OER, the OER involves a four-electron transfer and is the key process that governs overall electrochemical water splitting. Of many oxides that have been studied for OER catalysis, IrO_2 and RuO_2 are in the pole position.^{11,12} The overall cost of noble metals and their availability have prompted many researchers to look actively for alternatives that are based on non-precious elements and could be cost-effective.^{13–16} One such alternative could be compounds based on borates. It has been showed that borates could be good electrocatalysts for the OER.^{17–19}

The borate compound $A_2Mg_2TeB_2O_{10}$ (A = Ba and Pb) appears to have an interesting structure.⁷ B is three coordinated and forms $[BO_3]$ isolated units, which link with octahedral Mg^{2+} ions forming $[Mg_2B_2O_{10}]_{\infty}^{10-}$ two dimensional layers. The layers are connected by $[TeO_6]^{6-}$ octahedra, forming a three-dimensional structure with voids, where Ba^{2+}/Pb^{2+} ions are located. Octahedral Mg^{2+} ions provide a good opportunity to substitute other transition elements, which can exhibit electrocatalytic behavior. In this paper, we explored the borate compound $A_2Mg_2TeB_2O_{10}$ (A = Ba and Pb) towards new colored materials as well as their photocatalytic^{20,21} and electrochemical behavior.

Framework Solids Laboratory, Solid State and Structural Chemistry Unit,
Indian Institute of Science, Bangalore – 560012, India. E-mail: snatarajan@iisc.ac.in

[†]Electronic supplementary information (ESI) available: Crystal structure and SEM-EDX elemental mapping (Fig. S1 and S2), Raman studies (Tables S1 and S2, Fig. S3), optical studies (Fig. S4–S9, Table S3), stability studies (Fig. S10–S12), OER studies (Fig. S13–S20, Table S5), photocatalytic studies (Fig. S21–S26, Tables S6–S9). See DOI: <https://doi.org/10.1039/d4dt02706j>

[‡]These authors are equally contributed to this work.

Experimental section

Stoichiometric quantities of the respective metal salts and oxides were weighed and mixed using a pestle and mortar. A 10% excess of boric acid was taken in the initial mixture to compensate for possible losses at the elevated temperature. The synthesis was carried out by employing the solid-state technique. The starting mixtures were heated in the temperature ranges of 800–900 °C for 12–24 h duration with many intermittent grindings.

The prepared samples were characterised by powder X-ray diffraction (PXRD) (PANalytical Empyrean-X-ray diffractometer using nickel filtered Cu K α ($\lambda = 1.5417$ Å) in the 2θ range of 10° – 80° with a step size 0.02°). The observed PXRD patterns were compared with the simulated PXRD pattern of the Ba₂Mg₂TeB₂O₁₀ structure (Fig. 1).⁷ The compositional analysis was carried out using energy-dispersive X-ray (EDX) spec-

troscopy (SEM-EDX) and elemental mapping was carried out using a JEOL SEM IT300 instrument.

For the Rietveld refinement of the prepared compounds the PXRD data was collected at room temperature in the 2θ range of 10 – 120° with a step size of 0.02° and step duration of 50 s. The Rietveld refinements for the selected compounds were carried out using GSAS-II program.^{22,23} The lattice parameters, scale factors, background (Fourier polynomial background function), pseudo-Voigt (U, V, W, and X), and isothermal temperature factors (U_{iso}) were refined. Thermal parameters were constrained to be the same for the atoms occupying the same sites. The optical absorption and NIR reflectance for all the samples were recorded at room temperature (PerkinElmer Lambda 950 UV/vis double beam spectrometer, range of 200–2500 nm). X-ray photoelectron spectroscopy (XPS) was used to determine the oxidation states of the ions. Dielectric measurements [Novocontrol impedance analyzer (Alpha-A)] were carried out in the frequency range 10^5 Hz– 0.1 Hz at room temperature. Raman spectroscopic studies (HORIBA Lab RAM HR Evolution) were carried out in the range of 50 to 1400 cm⁻¹. ¹H NMR spectra were recorded on a Bruker instrument. The chemical shifts were relative to the CDCl₃.

The electrochemical performance of (Ba_{0.5}Pb_{1.5})(MgCo)TeB₂O₁₀ was studied employing a PARSTAT analytical electrochemical workstation (PAR) using the three-electrode system. The glassy carbon along with the catalyst was employed as the working electrode, the Hg/HgO electrode was employed as the reference electrode and a graphite rod was employed as the counter electrode. The electrolyte was 0.5 M KOH. The electrocatalytic performance towards the OER was evaluated employing an overpotential 10 mA cm⁻².²⁴

The photocatalytic reactions were performed by employing a modified procedure.^{20,21} A 20 mg of the photocatalyst (Ba₂(Mg_{1.5}Cu_{0.5})TeB₂O₁₀), in acetonitrile (3 mL) along with 1 : 3 ratio of vinyl arene and acetyl chloride were taken in a 10 mL round-bottom flask. The RB flask along with the oxygen balloon was placed under a 60 W LED bulb at room temperature and the reaction was carried out for 12 h under constant stirring. The progress of the reaction was monitored by thin-layer chromatography (TLC). After the completion of the reaction, the compound was isolated by column chromatography using silica gel and a mixture of hexane and ethyl acetate as the eluent.

Results and discussion

Synthesis and structural characterization

The compounds, A₂Mg₂TeB₂O₁₀ (A = Ba, Pb) have been reported earlier (Fig. S1[†]). The main feature of the structure is the framework [Mg₂TeB₂O₁₀]⁴⁻ having voids where the Ba²⁺/Pb²⁺ ions reside. We made attempts to prepare newer analogues of the structure by substituting Mg²⁺ ions (octahedrally coordinated) with other transition elements, which may give rise to interesting-colored compounds under day light.

All the compounds were prepared by solid-state methods and characterized by the PXRD method. The list of the pre-

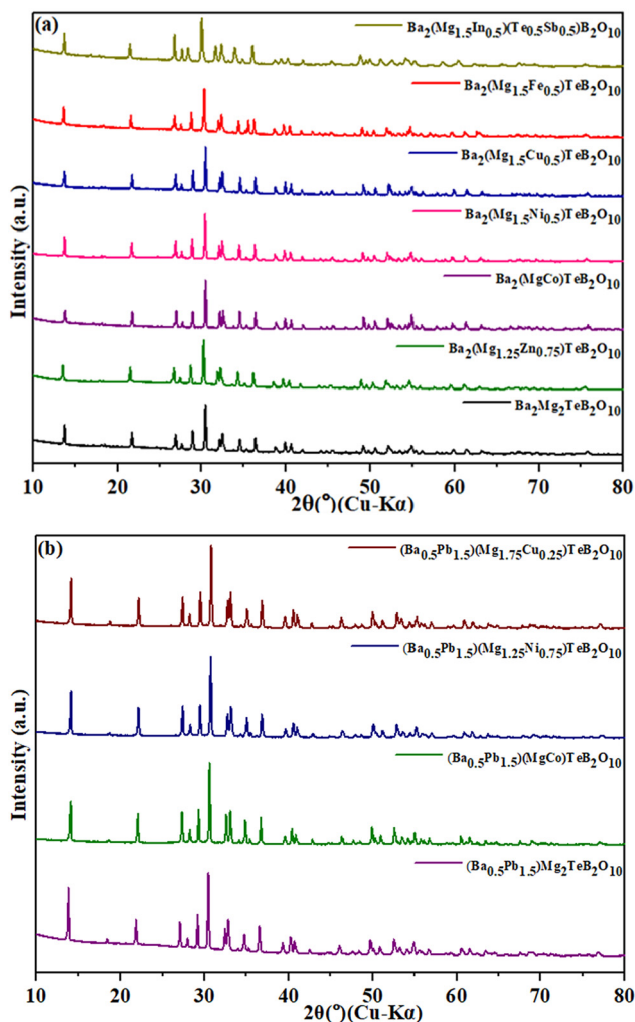


Fig. 1 (a) PXRD patterns of the Ba₂(Mg_{2-x}M_x)TeB₂O₁₀ (M = Co, Ni, Cu, Fe, and Zn) and (b) (Ba_{0.5}Pb_{1.5})(Mg_{2-x}M_x)TeB₂O₁₀ (M = Co, Ni, and Cu) compounds.

Table 1 Synthesis conditions for the prepared compounds

Compounds	Temperature (°C)/time (h)	Color as seen under daylight
Ba ₂ Mg ₂ TeB ₂ O ₁₀	800/12; 840/12	
Ba ₂ Mg _{1.25} Zn _{0.75} TeB ₂ O ₁₀	800/12; 840/12	
Ba ₂ MgCoTeB ₂ O ₁₀	900/12	
Ba ₂ Mg _{1.50} Ni _{0.50} TeB ₂ O ₁₀	870/12; 900/12	
Ba ₂ Mg _{1.50} Cu _{0.50} TeB ₂ O ₁₀	870/12; 900/12	
Ba ₂ Mg _{1.50} Fe _{0.50} TeB ₂ O ₁₀	850/12; 920/12	
Ba ₂ Mg _{1.50} In _{0.50} Te _{0.50} Sb _{0.50} B ₂ O ₁₀	800/12; 840/12	
Ba _{0.50} Pb _{1.50} Mg ₂ TeB ₂ O ₁₀	800/12	
Ba _{0.50} Pb _{1.50} MgCoTeB ₂ O ₁₀	820/12; 840/12	
Ba _{0.50} Pb _{1.50} Mg _{1.25} Ni _{0.75} TeB ₂ O ₁₀	800/12; 840/12	
Ba _{0.50} Pb _{1.50} Mg _{1.75} Cu _{0.25} TeB ₂ O ₁₀	800/12	

pared compounds is given in Table 1. The compound, Ba₂(MgCo)TeB₂O₁₀, was refined using the Ba₂Mg₂TeB₂O₁₀ structure as the model (Fig. 2).⁷

The structure of Ba₂(MgCo)TeB₂O₁₀ comprises (MgCo)B₂O₁₀ layers connected by TeO₆ octahedra forming a three-dimen-

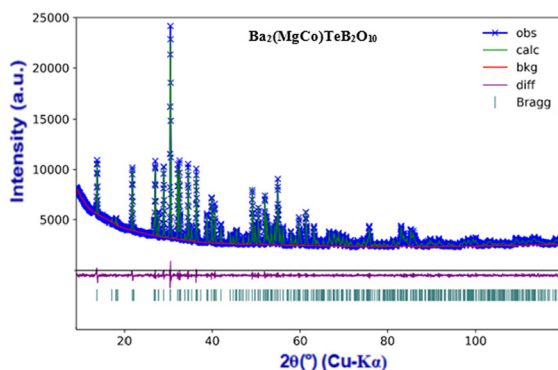


Fig. 2 Rietveld refinement of Ba₂(MgCo)TeB₂O₁₀ from the PXRD data. The observed (x), calculated (green line), and difference (bottom cyan line) profiles are shown. The vertical bars (|) indicate Bragg reflections.

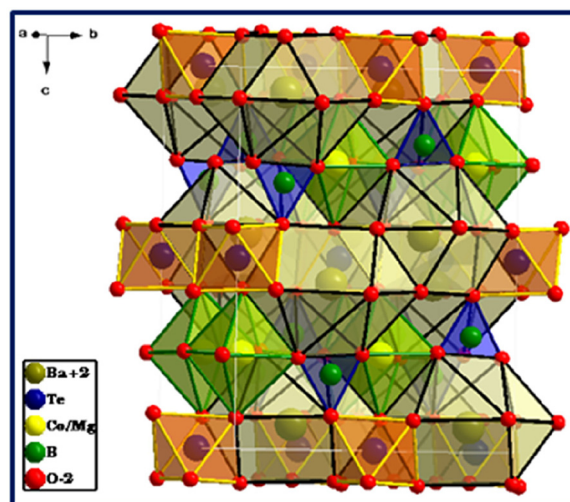


Fig. 3 Crystal structure of Ba₂(MgCo)TeB₂O₁₀ drawn from Rietveld refinement.

Table 2 Crystallographic data of Ba₂(MgCo)TeB₂O₁₀

Atom	Site	<i>x/a</i>	<i>y/b</i>	<i>z/c</i>	S.O.F.	<i>U</i> _{iso}
Ba1	8 f	0.5	0.1635(9)	0.4348(1)	1.0	0.0052(9)
Te1	4 b	0.0	0.0	0.5	1.0	0.0033(2)
Mg1	8 e	0.25	0.0866(3)	0.75	0.5	0.0051(9)
Co1	8 e	0.25	0.0866(3)	0.75	0.5	0.0051(9)
B1	8 f	0.0	0.1681(9)	0.3021(3)	1.0	0.0056(5)
O1	8 f	0.5	0.0487(4)	0.2528(3)	1.0	0.0043(4)
O2	16 g	0.2257 (9)	0.0826(4)	0.5812(9)	1.0	0.0087(9)
O3	8 f	0.0	0.1580(2)	0.4105(5)	1.0	0.0091(1)
O4	8 f	0.0	0.2799(8)	0.2561(6)	1.0	0.0037(1)

Space group: *Cmca* (64); *a* = 6.1997(5) Å; *b* = 10.4030 (4) Å; *c* = 12.9452 (4) Å; $\alpha = \beta = \gamma = 90^\circ$; *Z* = 4; *V* = 834.929 Å³. Reliability factors: *R*_p = 1.77%, *R*_{wp} = 2.38%, $\chi^2 = 1.94$. Bond length: Ba–O: 2.896 Å (avg.); Te–O: 1.9698 Å (avg.); Mg/Co–O: 2.1209 Å (avg.); B–O: 1.3806 Å (avg.). $\Delta = 0.433$ [Mg/Co]. Δ is the polyhedral distortion parameter defined by $\Delta = 1/N \sum [(r_i - r)/r]^2 10^3$, where *N* is the number of bonds and *r*_i and *r* are individual and average bond lengths, respectively.

sional structure with voids, wherein the Ba²⁺ ions are located (Fig. 3).

All the bond distances are in the expected ranges (Table 2). We were successful in partially substituting Sb⁵⁺ ions in place of Te⁶⁺ ions (50%) by introducing In³⁺ ions in place of Mg²⁺ ions forming a Ba₂(Mg_{1.5}In_{0.5})(Te_{0.5}Sb_{0.5})B₂O₁₀ compound. The SEM and EDX analysis indicated that the prepared compounds show expected composition of the samples (Fig. S2†).

Raman spectroscopic studies

The prepared compounds were also characterised by Raman spectroscopic studies (Fig. 4). The main Raman bands were observed in the range of 130–1300 cm⁻¹. The telluroborates and their derivatives crystallize in the orthorhombic crystal system, (*Cmca* (no. 64)). The presence of a center of symmetry in the space group indicates that the IR active vibration modes and the Raman active modes are mutually exclusive. In the

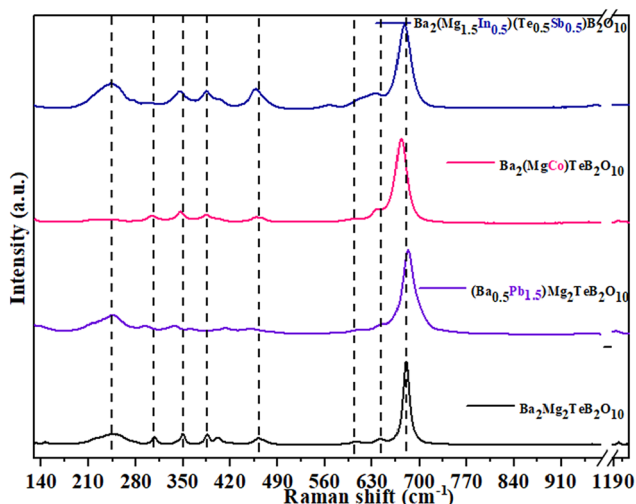


Fig. 4 Raman spectra for $(\text{Ba}_{2-x}\text{Pb}_x)(\text{Mg}_{2-x}\text{M}_x)\text{TeB}_2\text{O}_{10}$.

structure of $\text{Ba}_2\text{Mg}_2\text{TeB}_2\text{O}_{10}$, the Ba^{2+} ions have dodecahedral geometry and Mg^{2+} and Te^{6+} ions have octahedral geometry and the B^{3+} ions have triangular geometry. For all the ions, due to their multiplicities, a total of 102 modes can be observed, out of which 48 modes are expected to be Raman active based on the nuclear site group analysis (Table S1†).²⁵

$$\Gamma_{\text{total}}(102) = 14A_g + 10A_u + 10B_{1g} + 17B_{1u} \\ + 9B_{2g} + 16B_{2u} + 15B_{3g} + 11B_{3u}$$

$$\Gamma_{\text{Raman}}(48) = 14A_g + 10B_{1g} + 9B_{2g} + 15B_{3g}$$

The gerade symmetry modes, A_g , B_{1g} , B_{2g} , B_{3g} totalling 48 are Raman active and the ungerade B_{1u} , B_{2u} , B_{3u} symmetry modes (41 in total) are IR active, three ungerade B_{1u} , B_{2u} , and B_{3u} symmetry modes are acoustic and the ten A_u symmetry modes are optically inactive/silent modes. We did not observe all the expected Raman modes in our studies, which could be due to smaller intensity, overlapping of the modes and degeneracy.²⁶

Raman spectra for the parent compound $\text{Ba}_2\text{Mg}_2\text{TeB}_2\text{O}_{10}$ and the transition metal substituted ones $(\text{Ba}_2(\text{Mg}_{2-x}\text{M}_x)\text{TeB}_2\text{O}_{10})$, $\text{M} = \text{Fe}, \text{Co}, \text{Ni}, \text{Cu}, \text{Zn}$ indicate that the Raman bands are broader for the later (Fig. S3†). In addition, we observed a small shift in Raman bands compared to that in the parent compounds. The Raman spectra of the $\text{Ba}_2\text{Mg}_2\text{TeB}_2\text{O}_{10}$ compound were found to be sharper compared to that of the transition metal substituted ones $(\text{Ba}_2(\text{Mg}_{2-x}\text{M}_x)\text{TeB}_2\text{O}_{10})$, $\text{M} = \text{Fe}, \text{Co}, \text{Ni}, \text{Cu}, \text{Zn}$. We observed the Ba–O stretching modes in the range of $724\text{--}770\text{ cm}^{-1}$.²⁷

It is known that the isolated octahedra (MgO_6 and TeO_6) have six vibrational modes.^{28,29} Of these, three are Raman active (isolated TeO_6 : $A_{1g} \sim 600\text{--}700\text{ cm}^{-1}$; $E_g \sim 743\text{ cm}^{-1}$; $F_{2g} \sim 300\text{--}350\text{ cm}^{-1}$; MgO_6 : $A_{1g} \sim 479\text{--}516\text{ cm}^{-1}$; $E_g \sim 572\text{ cm}^{-1}$; $F_{2g} \sim 202\text{ cm}^{-1}$) and two are IR active and one is inactive towards both IR and the Raman. The Raman spectrum for

$\text{Ba}_2\text{Mg}_2\text{TeB}_2\text{O}_{10}$ compounds has the bands for TeO_6 octahedra in the range of $630\text{--}642\text{ cm}^{-1}$, which can be attributed to the symmetric stretching mode. The asymmetric stretching mode is observed at $724\text{--}770\text{ cm}^{-1}$. The bending vibration of TeO_6 octahedra is observed at $383\text{--}412\text{ cm}^{-1}$. For MgO_6 , the symmetric stretching mode was observed at $440\text{--}461\text{ cm}^{-1}$, the asymmetric stretching mode at $669\text{--}683\text{ cm}^{-1}$ and the bending modes at $204\text{--}222\text{ cm}^{-1}$. The BO_3 ion with a D_{3h} symmetry, has four fundamental modes, of which three are Raman-active ($A'_1 \sim 950\text{ cm}^{-1}$; $E' \sim 1250\text{--}1400\text{ cm}^{-1}$; $E'_1 \sim 600\text{ cm}^{-1}$) and one is infrared active.^{30,31} In the present compound, we observed the symmetric stretching mode in the range of $943\text{--}961\text{ cm}^{-1}$, the asymmetric stretching in the range of $1192\text{--}1208\text{ cm}^{-1}$ and the bending mode at $592\text{--}608\text{ cm}^{-1}$.

When the transition elements were substituted in $\text{Ba}_2(\text{Mg}_{2-x}\text{M}_x)\text{TeB}_2\text{O}_{10}$ ($\text{M}^{2+} = \text{Fe}/\text{Co}/\text{Ni}/\text{Cu}/\text{Zn}$), the Raman bands were found to be broader and shifted to higher wavenumbers (Table S2†).

For the compound, $\text{Ba}_2(\text{Mg}_{1.5}\text{In}_{0.5})(\text{Te}_{0.5}\text{Sb}_{0.5})\text{B}_2\text{O}_{10}$, the Raman bands appeared broader along with a small shift. Here the octahedral Te^{6+} ion shares the position with the Sb^{5+} ion and the Mg^{2+} ion shares the position with the In^{3+} ion. The observed Raman bands for Sb^{5+} and In^{3+} ions are: Sb^{5+}O_6 : $A_{1g} \sim 769\text{ cm}^{-1}$; $E_g \sim 581\text{ cm}^{-1}$; $F_{2g} \sim 381\text{ cm}^{-1}$; In^{3+}O_6 : $A_{1g} \sim 637\text{ cm}^{-1}$; $E_g \sim 540\text{ cm}^{-1}$; $F_{2g} \sim 308\text{ cm}^{-1}$.^{32,33}

As a part of the study, we partially replaced Ba^{2+} ions with Pb^{2+} ions. The compound, $\text{Pb}_2\text{Mg}_2\text{TeB}_2\text{O}_{10}$, has Pb^{2+} ions in a 5-coordinated position.⁷ When Pb^{2+} ions are substituted at the Ba^{2+} ions (11 coordinated) in $\text{Ba}_2\text{Mg}_2\text{TeB}_2\text{O}_{10}$, the Raman bands for the Ba–O were observed in the region of $140\text{--}145\text{ cm}^{-1}$ and the region of $286\text{--}291\text{ cm}^{-1}$ for Pb–O.

Dielectric measurements

We investigated the dielectric behavior of $\text{Ba}_2\text{Mg}_2\text{TeB}_2\text{O}_{10}$, $(\text{Ba}_{0.5}\text{Pb}_{1.5})\text{Mg}_2\text{TeB}_2\text{O}_{10}$, $\text{Ba}_2(\text{Mg}_{1.5}\text{In}_{0.5})(\text{Te}_{0.5}\text{Sb}_{0.5})\text{B}_2\text{O}_{10}$ compounds. The frequency dependence of the dielectric constant, ϵ' , and dielectric loss, $\tan \delta$, of the prepared compounds were measured at room temperature (Fig. 5).³⁴

We observed a dielectric constant value of 993 and $\tan \delta$ of 3.244 for $\text{Ba}_2\text{Mg}_2\text{TeB}_2\text{O}_{10}$ at low frequencies and the values start to decrease as the frequency is increased. The substitution of Pb^{2+} ions in place of Ba^{2+} ions in $(\text{Ba}_{0.5}\text{Pb}_{1.5})\text{Mg}_2\text{TeB}_2\text{O}_{10}$ gives rise to a slightly higher dielectric constant value of 1184 and $\tan \delta$ value of 2.755.³⁵ The substitution of Sb^{5+} ions in place of Te^{6+} ions in $\text{Ba}_2(\text{Mg}_{1.5}\text{In}_{0.5})(\text{Te}_{0.5}\text{Sb}_{0.5})\text{B}_2\text{O}_{10}$, resulted in a decrease in the overall dielectric behavior. Similar behavior has been observed before.³⁶

Normally, the dielectric behavior depends on the various polarizations in the compound such as the ionic, electronic, dipolar, and space charge. At lower frequencies, all the different components would contribute to the total polarizations and result in a larger value for the dielectric constant. As the applied field is increased, the different polarizations are relaxed out, which results in a decrease in the overall dielectric constant. This type of behavior is common in many ceramic oxides.³⁷ The present compounds, however, exhibited smaller

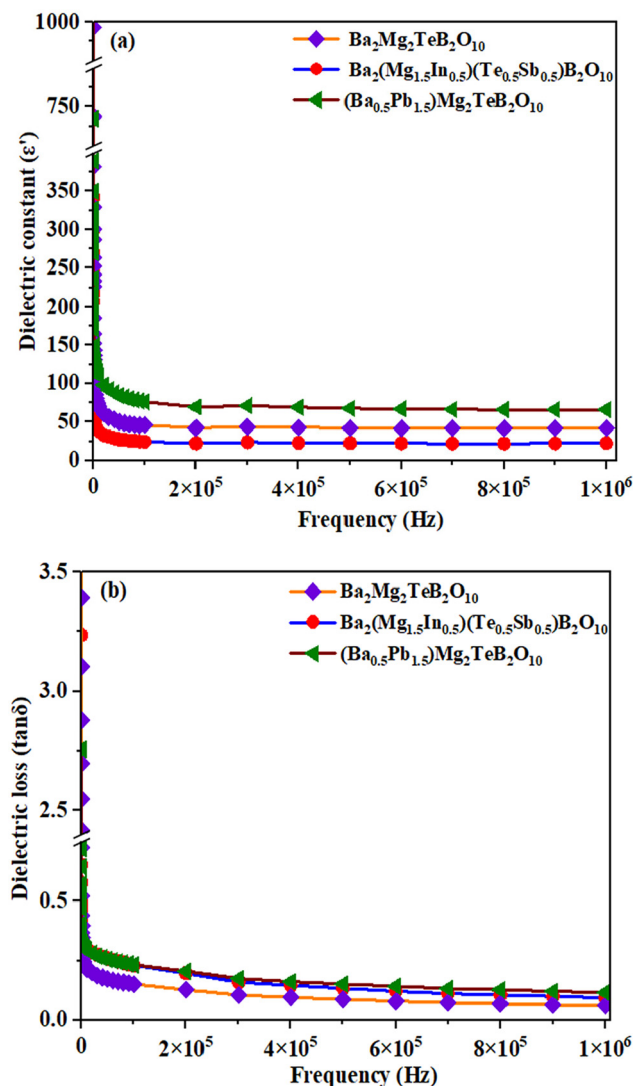


Fig. 5 (a) The dielectric constant and (b) dielectric loss versus frequency plots for the compounds at room temperature.

dielectric loss values, which may be beneficial towards their use in communication technologies.³⁸

Optical studies

The optical behavior of the compounds was investigated by employing UV-vis and near-IR spectroscopic studies. The transition metal substituted compounds exhibited colors that are expected for the transition elements in octahedral coordination (Table S3 and Fig. S4†).

The Co²⁺ substituted compound, Ba₂(Mg_{2-x}Co_x)TeB₂O₁₀ (0 < x ≤ 1) exhibits purple color under daylight. The optical absorption spectra exhibited one main absorption maxima at ~2.27 eV and another weak absorption at ~1.67 eV (Fig. 6).

The Co²⁺ ions in an octahedral coordination environment normally exhibit three spin-allowed transitions (1) ⁴T_{1g} → ⁴T_{2g}(F), (2) ⁴T_{1g} → ⁴A_{2g}(F), and (3) ⁴T_{1g} → ⁴T_{1g}(P).^{39,40} Of these, the ⁴T_{1g} → ⁴A_{2g}(F) and ⁴T_{1g} → ⁴T_{1g}(P) transitions are observed

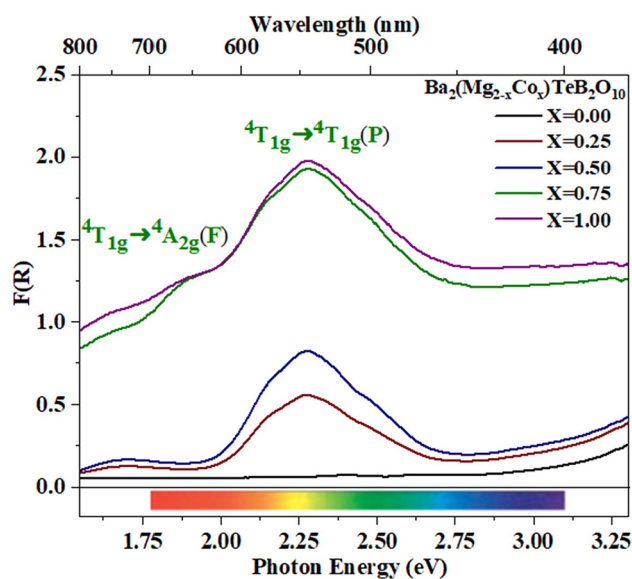


Fig. 6 Optical absorption spectra for Ba₂(Mg_{2-x}Co_x)TeB₂O₁₀ (0 < x ≤ 1).

in the visible region. The main absorption at ~2.27 eV (546 nm) may be due to the ⁴T_{1g} → ⁴T_{1g}(P) transition and the absorption at ~1.67 eV (742 nm) corresponds to the ⁴T_{1g} → ⁴A_{2g}(F) transition. In addition to the main absorption peaks at 2.27 eV, we observed two valleys on either side of the absorption band at ~1.9 eV (652 nm) and ~2.75 eV (450 nm). The combination of the absorption bands along with the valleys in the absorption spectra results in a purple color for the cobalt-substituted compounds.

The Ni²⁺ ions substituted Ba₂(Mg_{2-x}Ni_x)TeB₂O₁₀ (0 < x ≤ 0.5) exhibits a broad absorption at ~2.82 eV (Fig. 7). In addition, we also observed weak absorptions at ~2.40 eV,

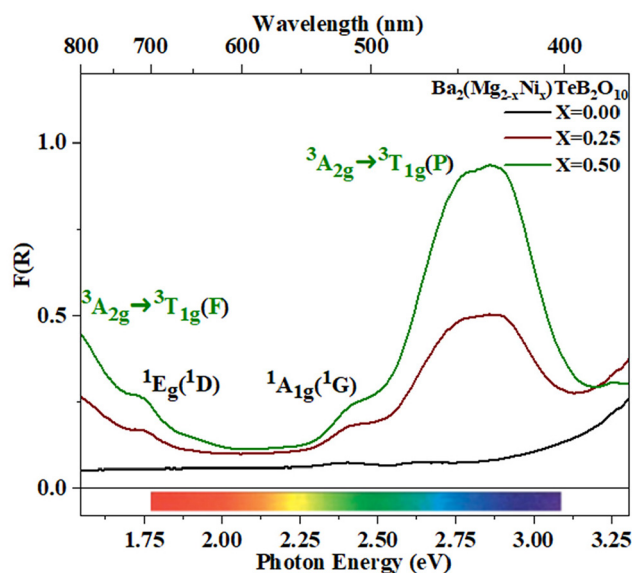


Fig. 7 Optical absorption spectra of Ba₂(Mg_{2-x}Ni_x)TeB₂O₁₀ (0 < x ≤ 0.5).

~ 1.74 eV and ~ 1.52 eV. The Ni-substituted compounds have a yellow-lime green color and the absorption spectra exhibit a deep valley of no absorption at ~ 2.1 eV (600 nm). The combination of the broad absorption band along with the valley gave rise to the yellow-lime-green color of the compounds. The Ni^{2+} ions in an octahedral environment have three transitions. (1) ${}^3\text{A}_{2g}({}^3\text{F}) \rightarrow {}^3\text{T}_{2g}({}^3\text{F})$, (2) ${}^3\text{A}_{2g}({}^3\text{F}) \rightarrow {}^3\text{T}_{1g}({}^3\text{F})$, and (3) ${}^3\text{A}_{2g}({}^3\text{F}) \rightarrow {}^3\text{T}_{1g}({}^3\text{P})$.^{39,40} Of these, the ${}^3\text{A}_{2g}({}^3\text{F}) \rightarrow {}^3\text{T}_{2g}({}^3\text{F})$ transition occur in the IR region. The main absorption at ~ 2.82 eV (439 nm) can be assigned to the ${}^3\text{A}_{2g}({}^3\text{F}) \rightarrow {}^3\text{T}_{1g}({}^3\text{P})$ transition and the weak absorption at ~ 1.52 eV (815 nm) could be due to the ${}^3\text{A}_{2g}({}^3\text{F}) \rightarrow {}^3\text{T}_{1g}({}^3\text{F})$. The shoulders at 2.40 eV (516 nm) and 1.74 eV (712 nm) could be due to the spin-forbidden transitions from ${}^3\text{A}_{2g}({}^3\text{F}) \rightarrow {}^1\text{A}_{1g}({}^1\text{G})$ ⁴¹ and ${}^3\text{A}_{2g}({}^3\text{F}) \rightarrow {}^1\text{E}_g({}^1\text{D})$.⁴²

The Cu^{2+} ions substituted $\text{Ba}_2(\text{Mg}_{2-x}\text{Cu}_x)\text{TeB}_2\text{O}_{10}$ ($0 < x \leq 0.50$) compounds exhibit different shades of green under daylight (Fig. S5†). The absorption spectra have a broad absorption at ~ 1.75 eV (708 nm). This absorption corresponds to the ${}^2\text{E}_g \rightarrow {}^2\text{T}_{2g}$ ($\text{Cu}^{2+}-d^9$) transition.⁴³ In addition, one can note a valley of low absorption in the region 2.2–2.5 eV. A combination of these results in the observed color for the Cu-substituted compounds. Similar behavior has been observed before.⁴⁴

The substitution of Fe^{2+} ions in $\text{Ba}_2(\text{Mg}_{2-x}\text{Fe}_x)\text{TeB}_2\text{O}_{10}$ ($0 < x \leq 0.5$) results in a brownish-red colored compound (Table S3†). The UV-vis spectra exhibit a broad absorption in the range of 2.00–2.50 eV with a peak centered at 2.25 eV (Fig. S6†). The Fe^{2+} ions in an octahedral environment normally exhibit one spin-allowed transition ${}^5\text{T}_{2g} \rightarrow {}^5\text{E}_g$ in the visible region.⁴⁵ The broad band centered at 2.25 eV (551 nm) corresponds to the ${}^5\text{T}_{2g} \rightarrow {}^5\text{E}_g$ transition.

As mentioned before, we have substituted the Pb^{2+} ions in place of Ba^{2+} ions in the compounds. It has been shown that the Pb^{2+} ion-containing compounds exhibited stronger and deeper colored compounds when transition elements are substituted.⁴⁶ Thus, the cobalt-substituted compounds $(\text{Ba}_{0.5}\text{Pb}_{1.5})(\text{Mg}_{2-x}\text{Co}_x)\text{TeB}_2\text{O}_{10}$ ($0 < x \leq 1$) were found to have a deeper purple color under daylight (Table S3†). Similar to the $\text{Ba}_2(\text{MgCo})\text{TeB}_2\text{O}_{10}$ compounds, the optical absorption spectra exhibited one main absorption maxima centered at 2.29 eV along with a shoulder at ~ 1.80 eV (Fig. 8). The main absorption at ~ 2.29 eV (541 nm) could be assigned to the ${}^4\text{T}_{1g} \rightarrow {}^4\text{T}_{1g}(\text{P})$ transition and the shoulder at ~ 1.80 eV (689 nm) corresponds to the ${}^4\text{T}_{1g} \rightarrow {}^4\text{A}_{2g}(\text{F})$ transition.

The Ni-substituted $(\text{Ba}_{0.5}\text{Pb}_{1.5})(\text{Mg}_{2-x}\text{Ni}_x)\text{TeB}_2\text{O}_{10}$ ($0 < x \leq 0.75$) compounds exhibit a broad absorption bands at ~ 2.91 eV and weak bands at ~ 2.47 eV, ~ 1.76 eV and ~ 1.57 eV (Fig. S7†). The compounds exhibited deeper yellow-lime green color. The main absorption at ~ 2.91 eV (426 nm) can be assigned to ${}^3\text{A}_{2g}({}^3\text{F}) \rightarrow {}^3\text{T}_{1g}({}^3\text{P})$ transition and the absorption at ~ 1.57 eV (789 nm) would be due to ${}^3\text{A}_{2g}({}^3\text{F}) \rightarrow {}^3\text{T}_{1g}({}^3\text{F})$. The shoulders at 2.47 eV (502 nm) and 1.76 eV (704 nm) may be due to the spin-forbidden transition from ${}^3\text{A}_{2g}({}^3\text{F}) \rightarrow {}^1\text{A}_{1g}({}^1\text{G})$ and ${}^3\text{A}_{2g}({}^3\text{F}) \rightarrow {}^1\text{E}_g({}^1\text{D})$.

The Cu^{2+} ions substituted compounds $(\text{Ba}_{0.5}\text{Pb}_{1.5})(\text{Mg}_{2-x}\text{Cu}_x)\text{TeB}_2\text{O}_{10}$ ($0 < x \leq 0.25$), exhibit different shades of

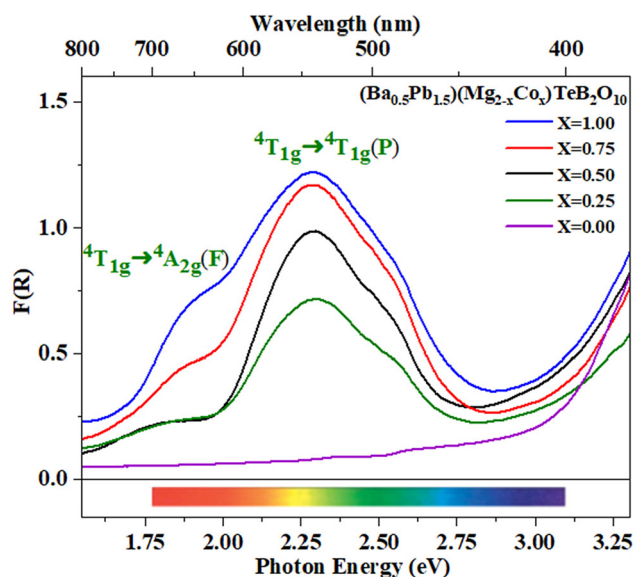


Fig. 8 Optical absorption spectra for $(\text{Ba}_{0.5}\text{Pb}_{1.5})(\text{Mg}_{2-x}\text{Co}_x)\text{TeB}_2\text{O}_{10}$ ($0 < x \leq 1$).

green color under daylight and the absorption spectra have close similarity to the Cu-substituted $\text{Ba}_2(\text{Mg}_{1.5}\text{Cu}_{0.5})\text{TeB}_2\text{O}_{10}$ compound (Fig. S8†).

We examined the NIR reflectance of the white-colored compounds (Fig. S9†).⁴⁷ All compounds, $\text{Ba}_2\text{Mg}_2\text{TeB}_2\text{O}_{10}$, $(\text{Ba}_{0.5}\text{Pb}_{1.5})\text{Mg}_2\text{TeB}_2\text{O}_{10}$, $\text{Ba}_2(\text{Mg}_{1.5}\text{In}_{0.5})(\text{Te}_{0.5}\text{Sb}_{0.5})\text{B}_2\text{O}_{10}$ and $\text{Ba}_2(\text{Mg}_{1.25}\text{Zn}_{0.75})\text{TeB}_2\text{O}_{10}$ exhibited good near IR reflectivity in the range of $\sim 75\%$, which is comparable to that of TiO_2 .

We also investigated the stability of the color of the prepared compounds by soaking them in hot water as well as 2 N HNO_3 for 24 h at room temperature. The tested samples did not exhibit any appreciable changes in the color, the PXRD patterns, and the UV-vis spectra (Fig. S10–S12†). This suggests that the compounds retain the color and are also stable.

Electrocatalytic studies

There has been a considerable surge in the development of electrocatalysts towards water oxidation studies in recent years.⁴⁸ In the present compounds, we successfully substituted Co^{2+} ions at the octahedral position in $\text{Ba}_2(\text{MgCo})\text{TeB}_2\text{O}_{10}$ and $(\text{Ba}_{0.5}\text{Pb}_{1.5})(\text{MgCo})\text{TeB}_2\text{O}_{10}$ compounds. We explored the possible electrocatalytic behavior of these two compounds towards the OER reaction under alkaline conditions.

The compound, $\text{Ba}_2(\text{MgCo})\text{TeB}_2\text{O}_{10}$, was added with acetylene carbon (4 : 1 ratio) and used as the electrode material. The OER reaction was investigated in the alkaline medium (0.5 M KOH), employing a three electrodes set-up where $\text{C-Ba}_2(\text{MgCo})\text{TeB}_2\text{O}_{10}$ -coated glassy carbon electrode (GC) acts as the working electrode, and a graphite rod and mercury/mercuric oxide (MMO) are used as the counter and reference electrodes, respectively (Fig. S13†). Prior to the electrochemical studies, the alkaline solution was purged for about 30 min by employing argon gas to remove any dissolved oxygen. The linear

sweep voltammetry (LSV) studies were carried out at a scan rate of 10 mV s^{-1} (Fig. 9a). The same experimental procedure was also followed for the $(\text{Ba}_{0.5}\text{Pb}_{1.5})(\text{MgCo})\text{TeB}_2\text{O}_{10}$ compound.

The OER activity of $\text{C}_{-}\text{Ba}_2(\text{MgCo})\text{TeB}_2\text{O}_{10}$ and $\text{C}_{-}(\text{Ba}_{0.5}\text{Pb}_{1.5})(\text{MgCo})\text{TeB}_2\text{O}_{10}$ compounds was investigated. A current density of 10 mA cm^{-2} along with the applied overpotential of 700 mV for $\text{C}_{-}\text{Ba}_2(\text{MgCo})\text{TeB}_2\text{O}_{10}$ was required, whereas an overpotential of 479 mV was sufficient for $\text{C}_{-}(\text{Ba}_{0.5}\text{Pb}_{1.5})(\text{MgCo})\text{TeB}_2\text{O}_{10}$ compounds for observing the OER activity. The relatively smaller overpotential for the $\text{C}_{-}(\text{Ba}_{0.5}\text{Pb}_{1.5})(\text{MgCo})\text{TeB}_2\text{O}_{10}$ compound suggested that the $\text{C}_{-}(\text{Ba}_{0.5}\text{Pb}_{1.5})(\text{MgCo})\text{TeB}_2\text{O}_{10}$ compound is better for the electrocatalytic behavior compared to the $\text{C}_{-}\text{Ba}_2(\text{MgCo})\text{TeB}_2\text{O}_{10}$ compound. Thus, we concentrated our studies on $(\text{Ba}_{0.5}\text{Pb}_{1.5})(\text{MgCo})\text{TeB}_2\text{O}_{10}$. The OER activity of the $\text{C}_{-}(\text{Ba}_{0.5}\text{Pb}_{1.5})(\text{MgCo})\text{TeB}_2\text{O}_{10}$ compound was also compared with IrO_2 (Fig. 9b). It appears that the OER activity of the

compound is comparable with IrO_2 and also to many other known compounds (Table S4†). The onset potential for $\text{C}_{-}(\text{Ba}_{0.5}\text{Pb}_{1.5})(\text{MgCo})\text{TeB}_2\text{O}_{10}$ compound is $\sim 1.53 \text{ V vs. RHE}$.

The Tafel slope gives an idea about the OER behavior. The Tafel polarization curve was measured in the low over-potential region and fitted to the Tafel equation (Fig. 10a). The Tafel slope was found to be $\sim 73 \text{ mV dec}^{-1}$, which is comparable to that observed for IrO_2 ($\sim 71 \text{ mV dec}^{-1}$). The low value of the Tafel slope suggested good activity towards the OER reaction.⁴⁹

The electrochemical AC impedance studies were carried out at the onset DC potential in the frequency range from 10 MHz to 100 kHz . The electrochemical impedance spectroscopy (EIS) was performed to learn about the charge transfer across the electrode–electrolyte interface (Fig. 10b).^{50–52} The experimental data of EIS were fitted with the equivalent circuit containing the solution resistance (R_s) and two parallel RC pairs along with the Warburg element (Fig. S14†).⁵³ R_s is the solution resistance, which has a contribution from the electrode and the electrolyte. The constant phase elements (CPE1 and CPE2), imply the presence of an imperfect capacitor in the system. The R_{int} and R_{ct} are the resistance from the polymeric film on the surface of the electrode and charge transfer resistance, respectively. The Warburg element (W) is required due to the diffusion of OH^- ion at the electrode–electrolyte interface. The charge transfer kinetics is inversely proportional to the charge transfer resistance (R_{ct}) and thus lower R_{ct} value indicates faster charge transfer. The R_{ct} measured from the Nyquist plot was found to be 94Ω , which suggests rapid charge transfer kinetics during the electrochemical process.

The long-term electrochemical stability of the catalyst was measured by employing chronoamperometry with the same applied potential (10 mA cm^{-2}) (Fig. 10c).⁵⁴ The studies indicated that the compound has good electrochemical stability for up to 18 hours. We carried out XPS investigations before and after the chronoamperometry studies. From the XPS studies, we observed that there is a partial oxidation of cobalt from the +2 to +3 state. After the chronoamperometry stability studies, we carried out the LSV measurements, which indicated a slight variation, which may be due to the partial oxidation of Co^{2+} to Co^{3+} in the compound (Fig. 10d). The electrochemical cyclability studies gave a value of $\text{Co}^{3+}/\text{Co}^{2+}$ ratio of 0.158 after 1000 cycles (Table S5, Fig. S15†).

The electrochemical active surface area of the catalyst was calculated from the double-layer capacitance (C_{dl}).⁵⁵ This was achieved by cyclic voltammetry by cycling the potential in the non-faradaic region at different scan rates from 5 to 120 mV s^{-1} .

The C_{dl} value is directly proportional to the conductivity and electrochemically effective surface area of the catalyst. The C_{dl} value was calculated from the slope of the plot between the scan rate and half the difference in the current density variation ($\Delta J = (1/2)(J_a - J_c)$) at 1.16 V vs. RHE (Fig. S16†). The ECSA value for the $\text{C}_{-}(\text{Ba}_{0.5}\text{Pb}_{1.5})(\text{MgCo})\text{TeB}_2\text{O}_{10}$ is 8.383 cm^2 .

The surface concentration and turnover frequency (TOF) of $\text{C}_{-}(\text{Ba}_{0.5}\text{Pb}_{1.5})(\text{MgCo})\text{TeB}_2\text{O}_{10}$ were calculated by linear scan voltammetric measurements with a scan rate of 10 mV s^{-1} in

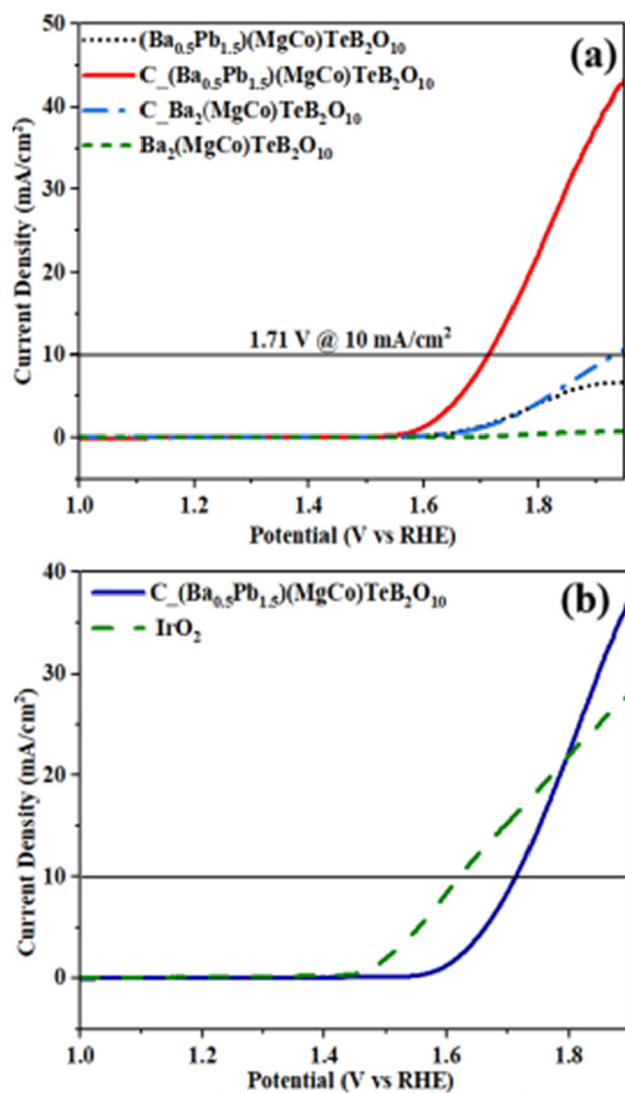


Fig. 9 (a) Linear sweep voltammogram (LSV) of cobalt substituted $(\text{Ba}_{0.5}\text{Pb}_{1.5})(\text{MgCo})\text{TeB}_2\text{O}_{10}$. (b) Comparison of the LSV plots of $\text{C}_{-}(\text{Ba}_{0.5}\text{Pb}_{1.5})(\text{MgCo})\text{TeB}_2\text{O}_{10}$ and IrO_2 .

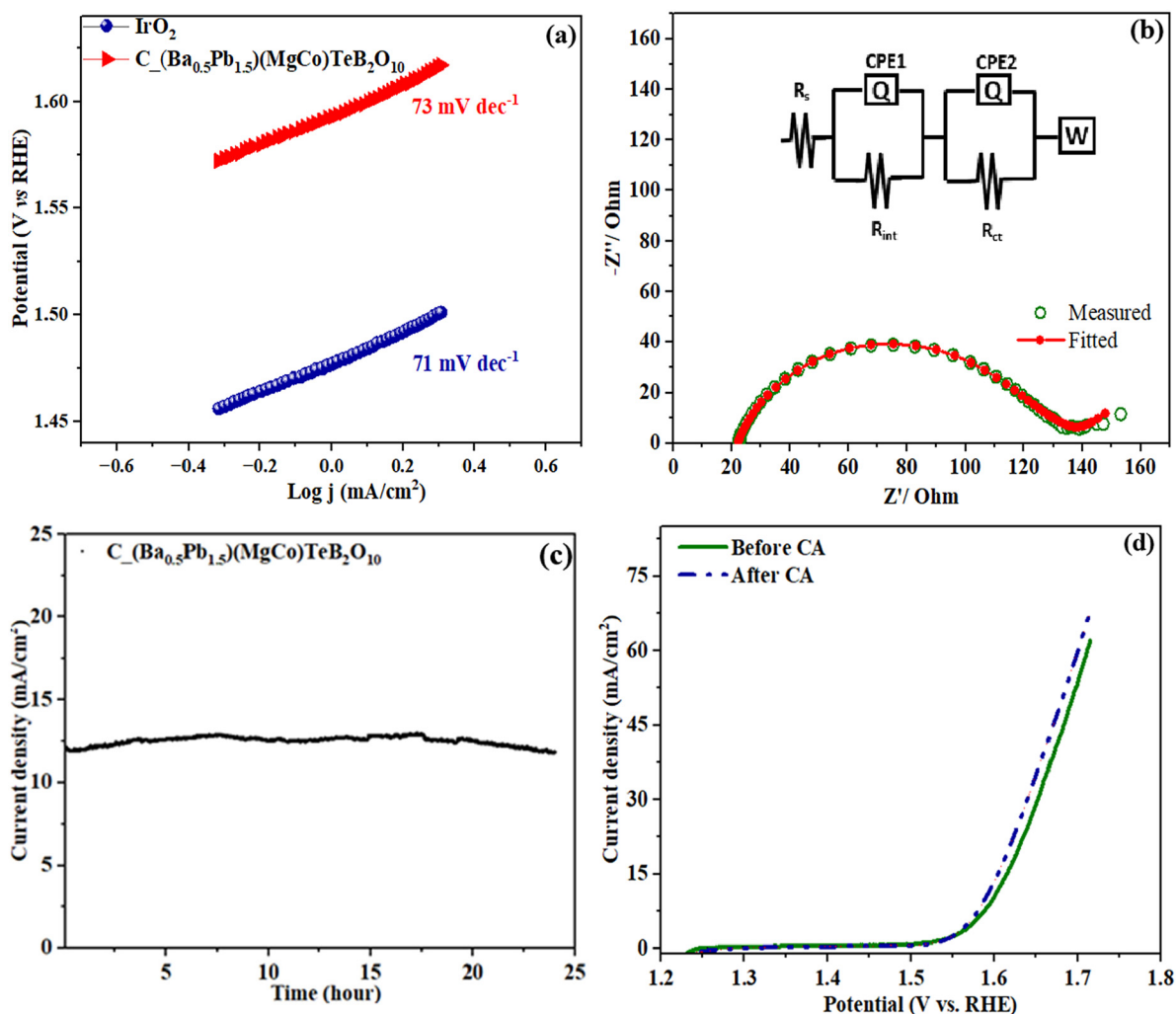


Fig. 10 (a) Tafel plot for the electrocatalyst derived from LSV plot. (b) Electrochemical impedance studies for the catalyst. (c) Chronoamperometric studies for stability for the catalyst. (d) LSV before and after chronoamperometric studies.

0.5 M KOH solution (Fig. S17[†]).⁵⁶ TOF is a measure of the conversion from the reactant to the product per catalyst site per unit time.⁵⁷ The calculated TOF was found to be 4.673 s^{-1} . Similar values have been observed before.⁵⁶

The faradaic efficiency (FE) of the electrocatalyst was investigated by employing an inverted burette to quantitatively measure the evolved oxygen as a function of time under constant DC bias. To this end, we employed a H-shaped electrochemical setup (Fig. S18[†]). The faradaic efficiency was estimated from the ratio between the moles of the oxygen gas produced experimentally and theoretically. We observed an evolution of $270.9 \mu\text{mol}$ of O_2 gas, which is in close agreement with the theoretical value ($279.8 \mu\text{mol}$). This indicates a faradaic efficiency of $\sim 96\%$ (Fig. S19[†]).⁵⁸

The stability of the electrocatalyst was determined by employing PXRD before and after the electrocatalytic studies (Fig. S20[†]). As can be noted, there is little change in the PXRD pattern suggesting that the compound did not undergo deterioration during the electrocatalytic studies.

Visible light-driven organic transformation

Mixed metal oxides have played an important role in the study of heterogeneous catalysis.⁵⁹ The use of TiO_2 , ZnO and other oxides towards photocatalytic purposes has been well established over the years.^{60,61} Similarly transition metal substituted compounds have also been explored towards photocatalytic organic transformations.⁶²

We explored visible light-activated organic transformations employing BiCdVO_5 and BiMgVO_5 compounds.⁶³ In the present study we observed a reduction in the band gap when transition metal ions are substituted for Mg^{2+} ions in $\text{Ba}_2\text{Mg}_2\text{TeB}_2\text{O}_{10}$. The compound, $\text{Ba}_2(\text{Mg}_{1.5}\text{Cu}_{0.5})\text{TeB}_2\text{O}_{10}$ has a band gap of $\sim 1.91 \text{ eV}$. It occurred to us that this compound may act as a photocatalyst. To investigate the photocatalytic activity, we attempted the oxidative halogenation reaction by employing visible light.⁶⁴

The aromatic α -chloroketones are important in many pharmaceuticals.^{65–67} The well-known methods for the syn-

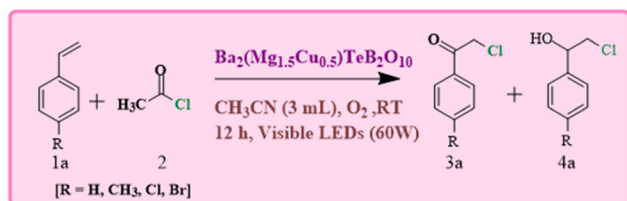
thesis of chloroketones are the direct halogenation of ketones, the oxidative halogenation of alkyne/alcohols and halogen exchange reactions.^{68–70} The conventional synthesis of α -haloketones generally involve employing molecular halogens or organic halogens ($\text{CH}_2\text{Cl}_2/N$ -halosuccinimide) along with a strong oxidant ($\text{ClO}_2/\text{K}_2\text{S}_2\text{O}_8$). In the present study, we attempted the halogenation employing acetyl chloride along

with molecular O_2 in the presence of visible light. This approach may be more advantageous as the Cu-centers can facilitate the formation of superoxide ($\cdot\text{OOH}$) radicals and halogen radicals ($\cdot\text{X}$), which may lead to good selectivity. In the photocatalytic oxochlorination of vinyl arenes, acetonitrile was employed as the solvent, which act to stabilize the co-ligand during the catalytic cycle.²¹

In the present study, we explored the oxidative halogenation by taking styrene and acetyl chloride as the substrate in acetonitrile in the presence of molecular oxygen under white light, 60 W LED, for 12 h. The photocatalytic reaction conditions were optimised with regard to reactants concentrations, solvent, catalyst quantity and the time of the reaction (Tables S6 and S7[†]). The reaction produced 2-chloro-1-phenylethan-1-one exclusively with a yield of ~75% (Scheme 1).

We carried out control experiments to establish the catalytic nature of this reaction. To this end, we explored reactions without (i) catalyst, (ii) light source, (iii) oxygen and (iv) acetyl chloride. In all the cases, no desired product was observed (Table S8[†]).

The catalytic reaction has expanded the scope of the study by exploring different substrates. The studies indicated that



Scheme 1 The optimized reaction of photocatalytic oxidative chlorination of vinyl arenes.

Table 3 Substrate scope: synthesis of α -chloroketones photocatalyzed by $\text{Ba}_2(\text{Mg}_{1.5}\text{Cu}_{0.5})\text{TeB}_2\text{O}_{10}$ under visible light. LED irradiation for 12 h

Entry	Reactant	Main product	Byproduct
1			
	1a	3a, 75%	4a, trace
2			
	1b	3b, 65%	4b, 8%
3			
	1d	3d, 71%	4d, 5%
4			
	1c	3c, 80%	4c, trace

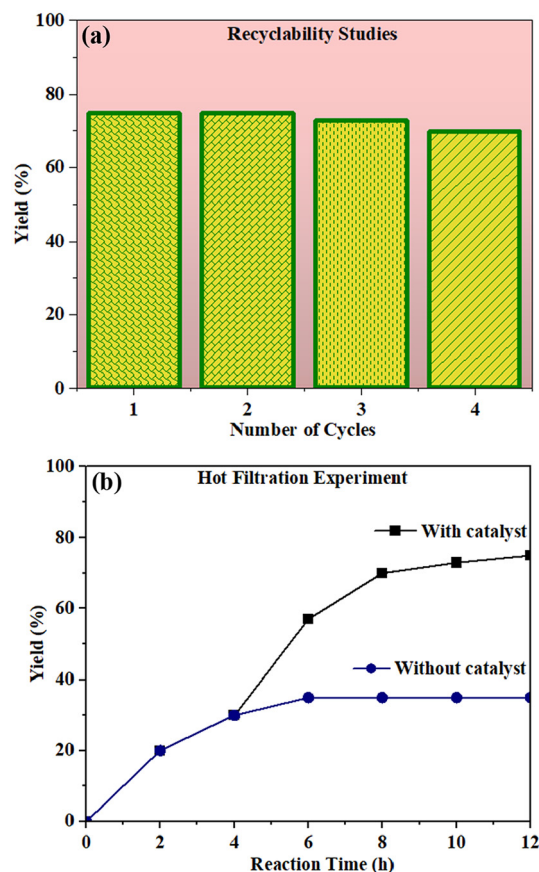


Fig. 11 (a) The recyclability studies of photocatalyst for oxochlorination of vinyl arenes. (b) Hot filtration experiment of photocatalytic oxidative halogenation of vinyl arenes. (■) reaction progress in the presence of the photocatalyst. (●) the percentage yield when the photocatalyst was removed via centrifugation after 4 h.

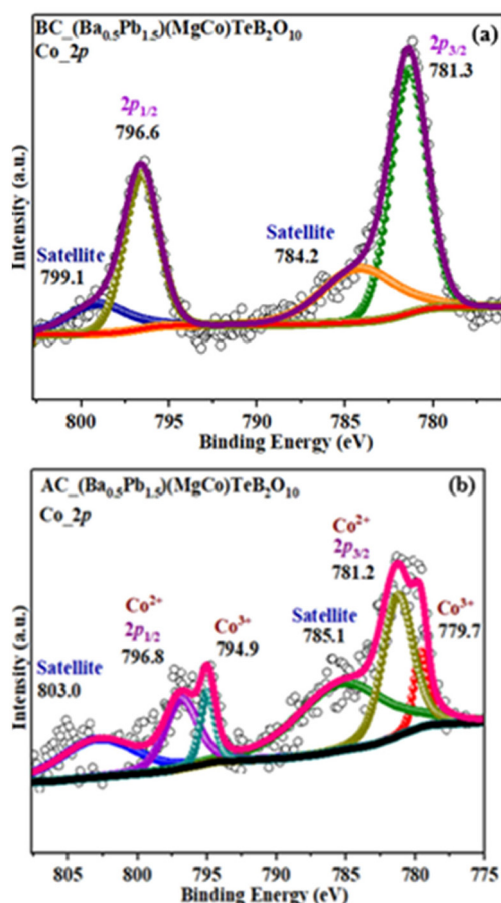


Fig. 12 X-ray photoelectron spectroscopy (XPS) for $(\text{Ba}_{0.5}\text{Pb}_{1.5})(\text{MgCo})\text{TeB}_2\text{O}_{10}$ before (a) and after (b) electrocatalysis.

the electron-withdrawing groups give better yields compared to the electron-donating group (Table 3). It is likely that the electron-withdrawing group may stabilise the α -carbon radical, facilitating the reaction with the photogenerated oxygen radicals ($\cdot\text{OOH}$). Similar observations have been made before.⁶⁴

The recyclability test for the photocatalyst was examined by repeating the experiment (Fig. 11a). We observed that the catalyst was stable for up to 4 cycles without losing much of the catalytic activity (Fig. S21†). We also carried out the hot filtration studies. For this, the catalyst was removed from the reaction mixture after 4 h by centrifugation and the filtrate was used to continue the reaction for 12 h under the same conditions. We found that the reaction did not proceed in the absence of the catalyst (Fig. 11b).

We proposed a possible pathway for the formation of the α -chloro ketone derivatives, which is based on earlier observations⁶⁴ (Fig. S22†). The photoactivation of the Cu-centers helps in the formation of chlorine radicals through light-induced homolysis. The formed chlorine radical then attacks the styrene forming the secondary benzylic radical. The benzylic radical reacts with the molecular oxygen to form the 2-chloroacetophenone. At the same time, the liberated proton from the reaction gives rise to water by the reduction of

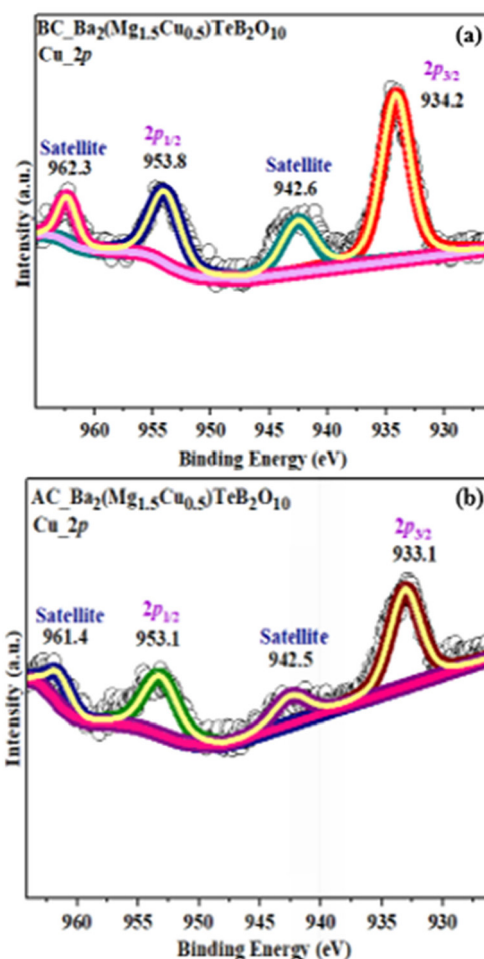


Fig. 13 XPS spectra of $\text{Ba}_2(\text{Mg}_{1.5}\text{Cu}_{0.5})\text{TeB}_2\text{O}_{10}$ before (a) and after (b) photocatalysis. The data points (O) are experimentally observed while the continuous light-yellow lines (—) are fitted curves.

molecular oxygen. The overall photocatalytic activity of $\text{Ba}_2(\text{Mg}_{1.5}\text{Cu}_{0.5})\text{TeB}_2\text{O}_{10}$ appears to be comparable to some of the reported compounds (Table S9†).

XPS studies

X-ray photoelectron spectroscopic (XPS) studies were carried out to investigate the oxidation state of cobalt in the compound before and after the electrocatalytic studies (Fig. 12). The Co 2p spectra of the $(\text{Ba}_{0.5}\text{Pb}_{1.5})(\text{MgCo})\text{TeB}_2\text{O}_{10}$ exhibits Co 2p_{3/2} peak at ~ 781.3 eV and Co 2p_{1/2} peak around 796.6 eV, along with the satellite features at ~ 784.2 eV and ~ 799.1 eV. These are typical values for Co^{2+} ions. After the electrocatalytic studies, the XPS studies indicated the presence of two additional peaks at ~ 779.7 eV and ~ 794.9 eV, which may be due to the Co 2p_{3/2} and Co 2p_{1/2} peaks, respectively, of Co^{3+} ions. A similar value for Co^{3+} ions has been noted earlier.⁷¹

The oxidation state of copper in the $\text{Ba}_2(\text{Mg}_{1.5}\text{Cu}_{0.5})\text{TeB}_2\text{O}_{10}$ compound was examined before and after the photocatalyst studies (Fig. 13). The Cu 2p spectra exhibit a Cu 2p_{3/2} peak at ~ 934.2 eV and a Cu 2p_{1/2} peak around ~ 953.8 eV, along with

the satellite features at ~ 942.6 eV and ~ 962.3 eV. These are typical values for Cu^{2+} ions.⁷² After the photocatalytic studies, the XPS studies did not exhibit any change in the Cu 2p spectra, which suggests that the catalyst was stable.

Conclusions

A series of telluroborates of the general formula, $\text{A}_2\text{M}_2\text{TeB}_2\text{O}_{10}$ (A = Ba, Pb; M = Mg, Zn, Co, Ni, Cu, Fe) were prepared and their properties investigated. The substitution at the bivalent octahedral positions by bivalent transition elements gave rise to compounds exhibiting interesting colors. The white-colored compounds exhibited NIR reflectivity values that are comparable to the commercial NIR compound, TiO_2 . The dielectric behavior of the white compounds exhibited reasonable values at low frequencies with low dielectric loss. The exploration of Co-substituted compounds towards OER activity in an alkaline medium was fruitful with $(\text{Ba}_{0.5}\text{Pb}_{1.5})(\text{MgCo})\text{TeB}_2\text{O}_{10}$ exhibiting OER activity that is comparable to IrO_2 . This compound exhibits 96% faradaic efficiency. The $\text{Ba}_2(\text{Mg}_{1.5}\text{Cu}_{0.5})\text{TeB}_2\text{O}_{10}$ compound, with a band gap of ~ 1.91 eV, was found to be a good visible light-activated photocatalyst for the formation of α -chloroketones. The study highlights the utility of telluroborates towards many materials properties and more such investigations are presently underway.

Author contributions

SS contributed to the synthesis of the compounds and performed PXRD measurements and UV-visible optical characterization. The electrochemical and photochemical studies were carried out by IGS. The overall scientific problem was conceived by SN.

Data availability

This is to certify that the additional data that are connected with the above manuscript is available as part of the electronic ESI.†

Conflicts of interest

There are no conflicts to declare.

Acknowledgements

Prof. S. N. thanks the Science and Engineering Research Board (SERB), Government of India, for the award of a research grant as well as the J. C. Bose National fellowship. We are thankful to Prof. Rajeev Ranjan for his help with dielectric studies. We thank Dr H. C. Sudeeksha and the Horiba facility for help with the Raman studies. IGS thanks Prof. S. Sampath for help with

the electrocatalytic studies. IGS also thanks the University Grants Commission (UGC), the Government of India and the Indian Institute of Science (IISc), for the research fellowship. Dr SS thanks DST-SERB for an NPDF (Grant No. PDF/2022/002873).

References

- 1 M. Mutailipu, K. R. Poeppelmeier and S. Pan, *Chem. Rev.*, 2020, **121**, 1130–1202.
- 2 P. Becker, *Adv. Mater.*, 1998, **10**, 979–992.
- 3 E. L. Belokoneva, *Crystallogr. Rev.*, 2005, **11**, 151–198.
- 4 T. T. Tran, H. Yu, J. M. Rondinelli, K. R. Poeppelmeier and P. S. Halasyamani, *Chem. Mater.*, 2016, **28**, 5238–5258.
- 5 P. C. Burns, *Can. Mineral.*, 1995, **33**, 1167–1176.
- 6 J. D. Grice, P. C. Burns and F. C. Hawthorne, *Can. Mineral.*, 1999, **37**, 731–762.
- 7 M. Wen, H. Wu, C. Hu, Z. Yang and S. Pan, *Inorg. Chem.*, 2019, **58**, 11127–11132.
- 8 F. Liu, C. Shi, X. Guo, Z. He, L. Pan, Z. Huang, X. Zhang and J. Zou, *Adv. Sci.*, 2022, **9**, 2200307.
- 9 A. Raveendran, M. Chandran and R. Dhanusuraman, *RSC Adv.*, 2023, **13**, 3843–3876.
- 10 J. Song, C. Wei, Z.-F. Huang, C. Liu, L. Zeng, X. Wang and Z. J. Xu, *Chem. Soc. Rev.*, 2020, **49**, 2196–2214.
- 11 J. H. Montoya, L. C. Seitz, P. Chakthranont, A. Vojvodic, T. F. Jaramillo and J. K. Nørskov, *Nat. Mater.*, 2017, **16**, 70–81.
- 12 C. Wei, R. R. Rao, J. Peng, B. Huang, I. E. L. Stephens, M. Risch, Z. J. Xu and Y. Shao-Horn, *Adv. Mater.*, 2019, **31**, 1806296.
- 13 S. Anantharaj and V. Aravindan, *Adv. Energy Mater.*, 2020, **10**, 1902666.
- 14 F. Zeng, C. Mebrahtu, L. Liao, A. K. Beine and R. Palkovits, *J. Energy Chem.*, 2022, **69**, 301–329.
- 15 Y. Xiong and P. He, *J. Mater. Sci.*, 2023, **58**, 2041–2067.
- 16 L. Cui, W. Zhang, R. Zheng and J. Liu, *Chem. – Eur. J.*, 2020, **26**, 11661–11672.
- 17 M. Dincă, Y. Surendranath and D. G. Nocera, *Proc. Natl. Acad. Sci. U. S. A.*, 2010, **107**, 10337–10341.
- 18 D. K. Bediako, B. Lassalle-Kaiser, Y. Surendranath, J. Yano, V. K. Yachandra and D. G. Nocera, *J. Am. Chem. Soc.*, 2012, **134**, 6801–6809.
- 19 X. Ji, L. Cui, D. Liu, S. Hao, J. Liu, F. Qu, Y. Ma, G. Du, A. M. Asiri and X. Sun, *Chem. Commun.*, 2017, **53**, 3070–3073.
- 20 T. Mandal, N. Katta, H. Paps and O. Reiser, *ACS Org. Inorg. Au*, 2023, **3**, 171–176.
- 21 A. S. Mereshchenko, P. K. Olshin, A. M. Karimov, M. Y. Skripkin, K. A. Burkov, Y. S. Tveryanovich and A. N. Tarnovsky, *Chem. Phys. Lett.*, 2014, **615**, 105–110.
- 22 B. H. Toby and R. B. Von Dreele, *Powder Diffr.*, 2014, **29**, S2–S6.
- 23 L. B. McCusker, R. B. Von Dreele, D. E. Cox, D. Louër and P. Scardi, *J. Appl. Crystallogr.*, 1999, **32**, 36–50.

- 24 H. L. Tuller, *Mater. Renewable Sustainable Energy*, 2017, **6**, 1–16.
- 25 D. L. Rousseau, R. P. Bauman and S. P. S. Porto, *J. Raman Spectrosc.*, 1981, **10**, 253–290.
- 26 Y.-Y. Sun and S. Zhang, *J. Chem. Phys.*, 2016, **145**, 021102.
- 27 M. R. Chandana, B. R. R. Krushna, J. Malleshappa, K. Manjunatha, T.-E. Hsu, S. Y. Wu, S. C. Sharma, B. D. Prasad, B. Subramanian and H. Nagabhushana, *Mater. Today Sustainability*, 2023, **22**, 100397.
- 28 R. L. Frost, *Spectrochim. Acta, Part A*, 2009, **72**, 903–906.
- 29 S. Chandra, G. Kaur, S. Abhay, B. Shukla, V. Srihari, G. M. Bhalerao and R. Govindaraj, *J. Raman Spectrosc.*, 2024, **55**, 728–738.
- 30 N. Kononova, V. Shevchenko, A. Kokh, T. Nabeeva, D. Chapron, A. Maillard, A. Bolatov and B. Uralbekov, *Mater. Res.*, 2016, **19**, 834–838.
- 31 D. Kasproicz, T. Runka, K. Jaroszewski, A. Majchrowski and E. Michalski, *J. Alloys Compd.*, 2014, **610**, 600–605.
- 32 R. Mukherjee, S. Saha, A. Dutta and T. P. Sinha, *J. Alloys Compd.*, 2015, **651**, 222–229.
- 33 H. Thauern and R. Glaum, *Z. Anorg. Allg. Chem.*, 2004, **630**, 2463–2467.
- 34 W. B. Westphal and A. Sils, *Dielectric constant and loss data, MIT Tech. Report*, Air Force Materials Laboratory, Air Force Systems Command, 1972, vol. 72.
- 35 S. A. Larrégola, J. A. Alonso, J. C. Pedregosa, M. J. Martínez-Lope, M. Alguero, V. De la Peña-O'shea, F. Porcher and F. Illas, *Dalton Trans.*, 2009, 5453–5459.
- 36 S. J. Mills, U. Kolitsch, R. Miyawaki, L. A. Groat and G. Poirier, *Am. Mineral.*, 2009, **94**, 1012–1017.
- 37 A. Klein, *J. Am. Ceram. Soc.*, 2016, **99**, 369–387.
- 38 M. T. Sebastian, *Dielectric materials for wireless communication*, Elsevier, 2010.
- 39 A. B. P. Lever, *Inorganic Electronic Spectroscopy*, Elsevier, Amsterdam, 2nd edn, 1984, p. 557.
- 40 D. N. Sathyanarayana, *Electronic absorption spectroscopy and related techniques*, Universities Press, 2001.
- 41 M. Kozielski, I. Pollini and G. Spinolo, *J. Phys. C: Solid State Phys.*, 1972, **5**, 1253.
- 42 M. Llusar, E. García, M. T. García, V. Esteve, C. Gargori and G. Monrós, *J. Eur. Ceram. Soc.*, 2015, **35**, 3721–3734.
- 43 K. B. N. Sarma, B. J. Reddy and S. V. J. Lakshman, *Phys. Lett. A*, 1982, **92**, 305–308.
- 44 A. Bhim, J. Gopalakrishnan and S. Natarajan, *Eur. J. Inorg. Chem.*, 2018, **2018**, 2277–2284.
- 45 I. Fontana, A. Lauria and G. Spinolo, *Phys. Status Solidi B*, 2007, **244**, 4669–4677.
- 46 A. Bhim, W. Zhang, P. S. Halasyamani, J. Gopalakrishnan and S. Natarajan, *Inorg. Chem.*, 2019, **58**, 8560–8569.
- 47 P. Jeevanandam, R. S. Mulukutla, M. Phillips, S. Chaudhuri, L. E. Erickson and K. J. Klabunde, *J. Phys. Chem. C*, 2007, **111**, 1912–1918.
- 48 Y. Li, X. Du, J. Huang, C. Wu, Y. Sun, G. Zou, C. Yang and J. Xiong, *Small*, 2019, **15**, 1901980.
- 49 T. Shinagawa, A. T. Garcia-Esparza and K. Takanahe, *Sci. Rep.*, 2015, **5**, 13801.
- 50 A. R. C. Bredar, A. L. Chown, A. R. Burton and B. H. Farnum, *ACS Appl. Energy Mater.*, 2020, **3**, 66–98.
- 51 E. Laouini, M. Hamdani, M. I. S. Pereira, J. Douch, M. H. Mendonça, Y. Berghoute and R. N. Singh, *J. Appl. Electrochem.*, 2008, **38**, 1485–1494.
- 52 M. E. G. Lyons and M. P. Brandon, *J. Electroanal. Chem.*, 2009, **631**, 62–70.
- 53 D. A. Harrington and P. Van Den Driessche, *Electrochim. Acta*, 2011, **56**, 8005–8013.
- 54 R. Frydendal, E. A. Paoli, B. P. Knudsen, B. Wickman, P. Malacrida, I. E. L. Stephens and I. Chorkendorff, *ChemElectroChem*, 2014, **1**, 2075–2081.
- 55 D. M. Morales and M. Risch, *J. Phys.: Energy*, 2021, **3**, 34013.
- 56 S. Anantharaj, P. E. Karthik and S. Kundu, *Catal. Sci. Technol.*, 2017, **7**, 882–893.
- 57 Y. Yan, X. Ge, Z. Liu, J.-Y. Wang, J.-M. Lee and X. Wang, *Nanoscale*, 2013, **5**, 7768–7771.
- 58 V. Kiran, D. Mukherjee, R. N. Jenjeti and S. Sampath, *Nanoscale*, 2014, **6**, 12856–12863.
- 59 J. M. Thomas and W. J. Thomas, *Principles and practice of heterogeneous catalysis*, John Wiley & Sons, 2014.
- 60 O. M. Ishchenko, V. Rogé, G. Lamblin and D. Lenoble, *Semiconductor Photocatalysis-Materials, Mechanisms and Applications*, 2016, pp. 3–30.
- 61 K. Wetchakun, N. Wetchakun and S. Sakulsermsuk, *J. Ind. Eng. Chem.*, 2019, **71**, 19–49.
- 62 X. Lang, X. Chen and J. Zhao, *Chem. Soc. Rev.*, 2014, **43**, 473–486.
- 63 A. Bhim, S. Sasmal, J. Gopalakrishnan and S. Natarajan, *Chem. – Asian J.*, 2020, **15**, 3104–3115.
- 64 F. Han, D. Zhang, S. Salli, J. Ye, Y. Li, F. Rosei, X.-D. Wen, H. Niemantsverdriet, E. Richards and R. Su, *ACS Catal.*, 2022, **13**, 248–255.
- 65 X. Zhu, Y. Lin, J. San Martin, Y. Sun, D. Zhu and Y. Yan, *Nat. Commun.*, 2019, **10**, 2843.
- 66 K. Pchalek, A. W. Jones, M. M. T. Wekking and D. S. Black, *Tetrahedron*, 2005, **61**, 77–82.
- 67 A. W. Erian, S. M. Sherif and H. M. Gaber, *Molecules*, 2003, **8**, 793–865.
- 68 J. C. Lee, J. Y. Park, S. Y. Yoon, Y. H. Bae and S. J. Lee, *Tetrahedron Lett.*, 2004, **45**, 191–193.
- 69 Y. Jing, C. G. Daniliuc and A. Studer, *Org. Lett.*, 2014, **16**, 4932–4935.
- 70 P. Klahn, H. Erhardt, A. Kotthaus and S. F. Kirsch, *Angew. Chem., Int. Ed.*, 2014, **53**, 7913–7917.
- 71 S. Jung, C. C. L. McCrory, I. M. Ferrer, J. C. Peters and T. F. Jaramillo, *J. Mater. Chem. A*, 2016, **4**, 3068–3076.
- 72 J.-C. Dupin, D. Gonbeau, P. Vinatier and A. Levasseur, *Phys. Chem. Chem. Phys.*, 2000, **2**, 1319–1324.